Journal of Materials Chemistry C

ROYAL SOCIETY OF CHEMISTRY

PAPER

View Article Online
View Journal | View Issue

Cite this: J. Mater. Chem. C, 2022, 10, 4795

Boosting organic afterglow efficiency *via* triplet–triplet annihilation and thermally-activated delayed fluorescence†

Jiulong Zhang,‡ Jiuyang Li,‡ Xun Li, Shou Yuan, Yan Sun, Yunlong Zou, Yingtong Pan and Kaka Zhang *

Received 13th October 2021,
Accepted 1st January 2022

DOI: 10.1039/d1tc04903h

rsc.li/materials-c

Due to the spin-forbidden nature of organic phosphorescence, it is challenging to achieve high afterglow efficiency in room-temperature organic afterglow systems, especially for those with long afterglow emission wavelengths. Here we report the incorporation of triplet–triplet annihilation (TTA) and thermally-activated delayed fluorescence (TADF) mechanisms to significantly enhance the organic afterglow efficiency in dopant–matrix systems under ambient conditions. Difluoroboron β-diketonate (BF_2bdk) compounds are selected as luminescent dopants and designed with naphthalene functional groups to show a relatively strong tendency of intersystem crossing. 4-Methoxybenzophenone matrices are employed to facilitate intersystem crossing of BF_2bdk excited states *via* dipole–dipole interactions and meanwhile suppress nonradiative decay and quenching of BF_2bdk triplet excited states. Besides phosphorescence decay, the dopant–matrix systems exhibit additional pathways to harvest triplet energies *via* TTA and TADF, leading to the significant improvement of the organic afterglow efficiency. The afterglow materials can be melt-cast into desired shapes, can function as multicolor-encoded anti-counterfeiting objects, and can be processed into aqueous dispersions, which display background-free bioimaging properties.

Introduction

Manipulation of triplet excited states is of vital importance in diverse aspects of photofunctional systems such as room-temperature phosphorescence (RTP),[1–5] aggregation-induced emission,[6] triplet–triplet annihilation (TTA),[7–15] thermally activated delayed fluorescence (TADF),[16–23] and organic afterglow materials.[24–32] Recent years have witnessed very exciting advancements of room-temperature organic phosphorescence and afterglow materials, because these materials exhibit intriguing applications in microenvironment oxygen sensing, anti-counterfeiting, optical storage, bioimaging and sensors.[33–38] However, due to the spin-forbidden nature of phosphorescence, it remains a formidable task to achieve high afterglow efficiency (emission lifetime >0.1 s) in purely organic systems.

Pioneering studies have shown that judicious molecular design, aggregation state control, and supramolecular assembly can be used to control the properties of triplet excited states and improve the organic afterglow efficiency.[39–47] Recently, two-component dopant–matrix design strategies have been reported by our research group and others to exhibit strong capability in devising high-performance organic afterglow materials.[48–58] Through the manipulation of triplet excited state properties in the dopant–matrix systems, organic materials with high afterglow efficiency, ultralong afterglow lifetimes, and intense afterglow brightness have been achieved.[48–52] The dopant–matrix strategy also allows a very flexible choice of both luminescent dopants and organic matrices, giving rise to diverse organic afterglow materials with different compositions and intriguing properties.[48–52] Besides, two-component donor–acceptor systems based on retarded charge recombination have been reported to exhibit surprisingly long afterglow durations of up to hours.[53–56] These afterglow systems showed decreased performance when exposed to ambient conditions because of the instability of photogenerated radical cations and radical anions. The donor–acceptor systems have also been extended to the fabrication of aqueous afterglow materials and efficient afterglow materials with long emission wavelengths.[57,58]

Despite the above success, it is still challenging to fabricate highly efficient organic afterglow materials under ambient conditions, especially for those with long afterglow emission

Key Laboratory of Synthetic and Self-Assembly Chemistry for Organic Functional Molecules, Shanghai Institute of Organic Chemistry, University of Chinese Academy of Sciences, Chinese Academy of Sciences, 345 Lingling Road, Shanghai, 200032, People's Republic of China. E-mail: zhangkaka@sioc.ac.cn

† Electronic supplementary information (ESI) available: Experimental section, supporting figures. CCDC 2115255. For ESI and crystallographic data in CIF or other electronic format see DOI: 10.1039/d1tc04903h

‡ Equal contribution.

wavelengths.[24–38] Fig. S1 (ESI†) illustrates the current status of the research of organic afterglow materials where only a very small percentage of organic materials show both high afterglow efficiency and long emission lifetimes. Fig. S2 (ESI†) exhibits the chemical structures of selected high-performance organic afterglow materials, among which the afterglow emission wavelengths have been found to be mostly restricted to the range of 400 nm to 550 nm. To date, highly efficient afterglow materials with long emission wavelengths, for example, larger than 550 nm or 600 nm, remain rarely reported (Fig. S3 and S4, ESI†).

Besides the population of triplet excited states, harvesting triplet energies is another key to achieve high afterglow efficiency. Inspired by the fantastic achievements of TTA and TADF in the area of metal-complex-based systems and OLED research areas,[7–23] we conceive that, if the triplet excited states of organic afterglow systems can be harvested by TTA and TADF pathways, a drastic enhancement of the organic afterglow efficiency would result (Scheme 1). Different from conventional TTA and TADF material design,[7–23,59,60] moderate or modest rate constants of TTA and TADF (k_{TTA} and k_{TADF}) are required to maintain the afterglow emission lifetimes > 0.1 s; large k_{TTA} and k_{TADF} lead to drastic shortage of emission lifetimes. Since organic systems without the presence of heavy atoms typically possess phosphorescence rate constants (k_P) on the order of 10^{-2} to 10^{3} s^{-1}, moderate or modest values of k_{TTA} and k_{TADF} in the range of 10^{-1} to 10^{1} s^{-1} would be sufficient to open additional pathways to significantly harvest triplet energies and improve the afterglow efficiency (Scheme 1).

On the basis of the above consideration, here we design naphthalene-containing BF_2bdk luminescent dopants with relatively strong tendency of intersystem crossing and relatively low energy levels of excited states (Scheme 2). 4-Methoxybenzophenone (MeOBP) matrices are used to stabilize the singlet excited states of BF_2bdk *via* dipole–dipole interactions, reduce ΔE_{ST} given that the energy level of BF_2bdk triplets is less affected by organic matrices, and consequently facilitate both forward and reverse intersystem crossing of BF_2bdk excited states. At the same time, the organic matrices can suppress nonradiative decay of BF_2bdk triplets by their rigid microenvironment and protect BF_2bdk triplets from oxygen quenching by encapsulation. Because of the relatively large population of triplet excited states, TTA processes in NPhBF_2–MeOBP, NαNBF_2–MeOBP and NβNBF_2–MeOBP afterglow systems can be switched on to enhance the afterglow efficiency. It has been found that NPhRedBF_2–MeOBP afterglow materials exhibit a TADF-type organic afterglow mechanism with high efficiency and an emission wavelength of >600 nm. The organic afterglow materials have been found to display excellent processability into desired shapes and aqueous dispersions, which exhibit promising characteristics for advanced anti-counterfeiting and high-contrast bioimaging applications.

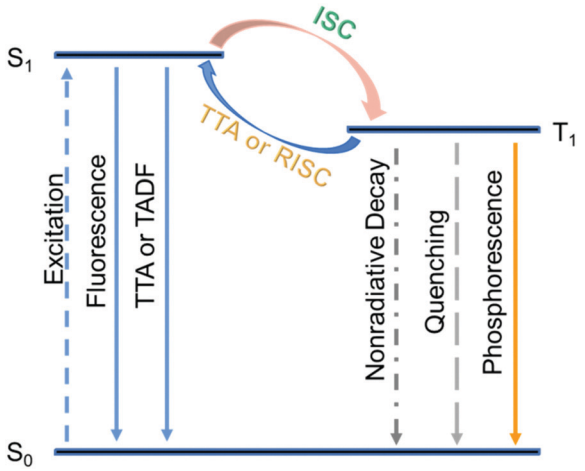

Scheme 1 Enhancing organic afterglow efficiency in dopant–matrix systems *via* TTA and TADF mechanisms.

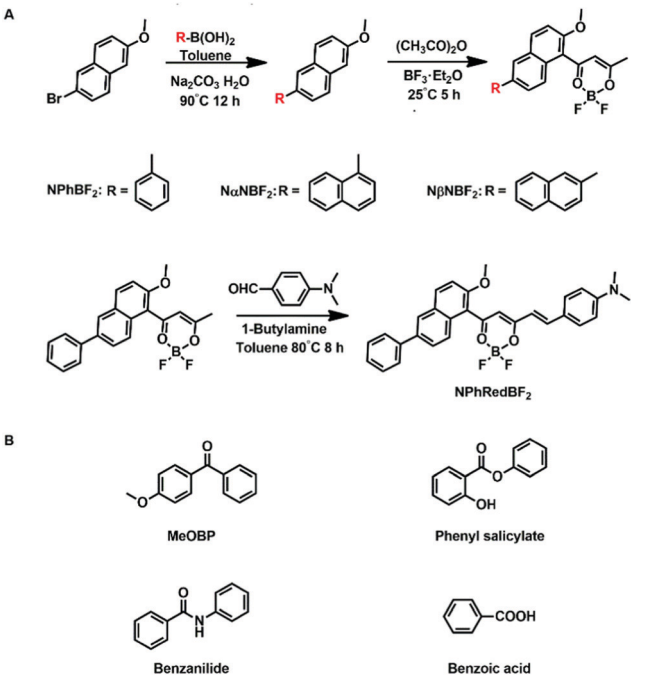

Scheme 2 Synthesis of naphthalene-containing BF_2bdk luminescent compounds *via* a cascade reaction and further modification.

Results and discussion

Design and synthesis of naphthalene-containing BF_2bdk luminescent compounds

The naphthalene system is known to possess high quantum yields of intersystem crossing (Φ_{ISC}) but relatively small molar absorption coefficient. In view of these, we decorate naphthalene substrates with BF_2bdk functional groups by the cascade reaction developed in our recent studies (Scheme 2)[61,62] to enhance their absorption in visible regions and maintain their high Φ_{ISC}. The cascade reaction of aromatic substrates in acetic anhydride and boron trifluoride diethyl etherate is very simple and straightforward, which can be successfully performed even without the use of Schlenk techniques. The naphthalene-

containing BF_2bdk luminescent compounds have been obtained with reasonable isolation yields. $NPhBF_2$ compounds were further allowed to react with 4-dimethylaminobenzaldehyde to form boron difluoride hemicurcuminoid compounds with larger aromatic conjugation lengths (Scheme 2) and consequently with lower singlet excited state energy levels for red afterglow materials (*vide infra*). The naphthalene-containing BF_2bdk luminescent compounds were structurally characterized by ^{1}H NMR, ^{13}C NMR, ^{19}F NMR, ^{11}B NMR, LRMS, HRMS, and single crystal X-ray diffraction (Fig. 1A), as well as UV-vis and steady-state emission studies (see ESI†).

Table 1 summarizes the photophysical properties of the naphthalene-containing BF_2bdk compounds in dilute solutions; UV-vis, emission spectra and excited state decay profiles are shown in Fig. S5–S7 (ESI†). $NPhBF_2$, $N\alpha NBF_2$ and $N\beta NBF_2$ in dichloromethane solutions show UV-vis absorption bands in the range of 360 nm to 460 nm (Fig. 1B), which can be assigned to intramolecular charge transfer (ICT) transition from aromatic groups to the dioxaborine moieties.[63,64] TD-DFT calculations, which show typical ICT characteristics in S_1 states, support these assignments (Fig. 1C). Given that the LUMO levels of the naphthalene-containing BF_2bdk compounds are fixed by dioxaborine functional groups, the absorption of naphthalene-containing BF_2bdk compounds in the visible regions can be attributed to the electron-rich nature of naphthalene functional groups. By extending the conjugation lengths of the naphthalene-containing electron-donating functional groups, $NPhRedBF_2$ compounds have been found to exhibit intense absorption bands ranging from 400 nm to 600 nm (Fig. 1B and C). Steady-state emission studies show that $NPhBF_2$, $N\alpha NBF_2$ and $N\beta NBF_2$ in dichloromethane solutions possess broad emission bands in the range of 425 nm to 650 nm, while $NPhRedBF_2$ display 550–750 nm emission bands with maxima at 606 nm (Fig. 1D and Fig. S6, ESI†).

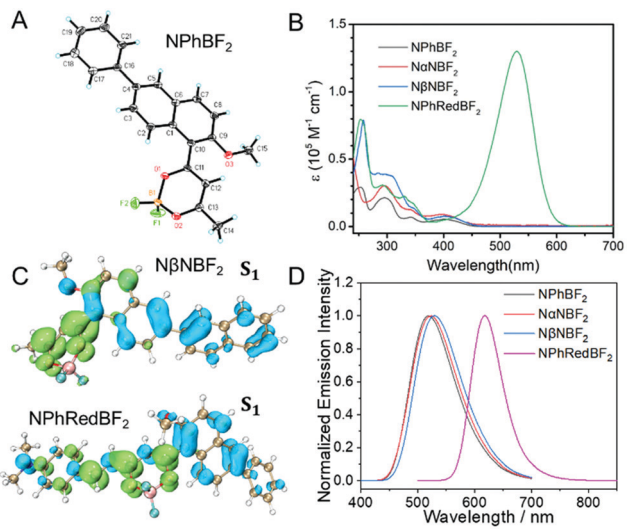

Fig. 1 (A) Single crystal structure of $NPhBF_2$. (B) UV-vis spectra of naphthalene-containing BF_2bdk in dichloromethane solutions. (C) TD-DFT calculated results of $N\beta NBF_2$ and $NPhRedBF_2$ S_1 states. Blue and green isosurfaces correspond to hole and electron distributions, respectively. TD-DFT calculations were performed in the ORCA 4.2.1 program with the B3LYP functional and def2-TZVP(-f) basis set. (D) Steady-state emission spectra of naphthalene-containing BF_2bdk in dichloromethane solutions.

Table 1 Photophysical data of naphthalene-containing BF_2bdk solutions at room temperature

Entry	λ_{abs} (nm)	λ_{em} (nm)	τ (ns)	Φ(%)
$NPhBF_2$ in dichloromethane	400	518	5.5	9.4
$NPhBF_2$ in tetrahydrofuran	391	493	8.6	35.1
$N\alpha NBF_2$ in dichloromethane	396	524	6.5	8.4
$N\alpha NBF_2$ in tetrahydrofuran	386	494	8.5	33.9
$N\beta NBF_2$ in dichloromethane	402	529	5.7	5.9
$N\beta NBF_2$ in tetrahydrofuran	394	500	9.2	30.4
$NPhRedBF_2$ in dichloromethane	528	618	0.9	15.5
$NPhRedBF_2$ in tetrahydrofuran	516	606	1.1	21.4

Afterglow material fabrication *via* a dopant–matrix design strategy

The naphthalene-containing BF_2bdk powders in the present study exhibit bright fluorescence upon excitation but show no room-temperature afterglow after removal of the excitation source (Fig. S8, ESI†). A dopant–matrix design strategy has been used for the fabrication of organic afterglow materials. Diverse organic matrices have been tested (Scheme 2B). The materials obtained by doping $N\beta NBF_2$ into MeOBP show the most significant afterglow properties with relatively high afterglow brightness and long afterglow durations (Fig. S9, ESI†); MeOBP matrices alone show insignificant room-temperature afterglow (Fig. S10, ESI†). Therefore, the organic matrices were fixed as MeOBP for the preparation of afterglow materials in the following studies. It is found that afterglow materials prepared by melt casting exhibit better afterglow performance than those obtained by a grinding method (Fig. 2, Fig. S11–S14, ESI†). The melt-cast $NPhBF_2$–MeOBP, $N\alpha NBF_2$–MeOBP, and $N\beta NBF_2$–MeOBP materials exhibit orange afterglow, while $NPhRedBF_2$–MeOBP materials display orange red afterglow under ambient conditions (Fig. S14, ESI†). At 77 K, the naphthalene-containing BF_2bdk powders show weak afterglow (Fig. S15, ESI†), whereas the BF_2bdk–MeOBP samples at 77 K exhibit significant organic

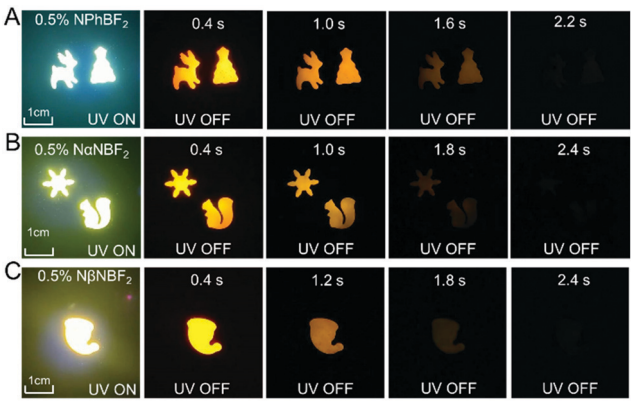

Fig. 2 Photographs of (A) $NPhBF_2$–MeOBP-0.5%, (B) $N\alpha NBF_2$–MeOBP-0.5% and (C) $N\beta NBF_2$–MeOBP-0.5% afterglow materials under 365 nm UV light and after removal of the UV light.

afterglow (Fig. S16, ESI†). These observations indicate the successful fabrication of afterglow materials by the dopant–matrix design strategy.

Photophysical studies of the BF_2bdk–MeOBP materials have been performed (Table 2 and Table S1, ESI†). $NPhBF_2$–MeOBP, $N\alpha NBF_2$–MeOBP, and $N\beta NBF_2$–MeOBP materials display 450–650 nm emission bands in the steady-state fluorescence spectra. The delayed emsision spectra show 550–750 nm phosphorescence bands and 450–530 nm delayed fluorescence bands with identical emission maxima to the fluorescence peak (Fig. 3A–C); dual emission has been observed.[65–67] Besides, it is found that the steady-state fluorescence spectra of $NPhBF_2$–MeOBP, $N\alpha NBF_2$–MeOBP, and $N\beta NBF_2$–MeOBP materials display red-shifted fluorescence maxima by increasing BF_2bdk doping concentrations (Fig. 3A–C), which suggest molecular aggregation of BF_2bdk in MeOBP matrices *via* π–π interactions. The phosphorescence maxima show insignificant changes upon the variation of the doping concentrations, which agrees well with the observations in phosphorescence spectra of other reported systems; the phosphorescence spectra of many organic compounds are insensitive to the states and the microenvironments of these organic compounds.[68]

The significant room-temperature phosphorescence can be attributed to the relatively strong tendency of intersystem crossing of the naphthalene-containing BF_2bdk luminescent compounds. TD-DFT calculations exhibit rich channels of S_1-to-T_n intersystem crossing with relatively large spin–orbit coupling matrix elements (Fig. 3E, F, Fig. S17, ESI†), some of which possess relatively small ΔE_{ST} values. Because of the relatively large population of BF_2bdk triplet excited states in the dopant–matrix systems, it is understandable that the delayed emission spectra of $NPhBF_2$–MeOBP, $N\alpha NBF_2$–MeOBP, and $N\beta NBF_2$–MeOBP materials exhibit 450–530 nm delayed fluorescence bands (Fig. 3C); $N\beta NBF_2$–MeOBP materials show the most significant delayed fluorescence bands (Fig. S18, ESI†). The relative intensity of the delayed fluorescence bands is found to increase with the BF_2bdk doping concentration, which suggests the formation of triplet–triplet annihilation in the dopant–matrix systems. TTA is a bimolecular process and increases with triplet concentrations. The double logarithmic plot of the emission decay profile of the $N\beta NBF_2$–MeOBP-0.5% sample monitored at 515 nm obeys a power law with a slope of −1.77 (Fig. 3G). With reference to the reported studies, these observations support that the 515 nm delayed emission bands are originated from bimolecular TTA processes (Fig. 3H).[7–15] It is also found that the delayed emission spectra of $N\beta NBF_2$ solution in dichloromethane at 77 K show weak delayed fluorescence signals in the range of 500 nm to 570 nm (Fig. S19, ESI†). These observations further support the involvement of TTA in the $N\beta NBF_2$ system.

Table 2 Photophysical data of BF_2bdk–MeOBP materials at room temperature

Entry	λ_{em} (nm)	τ (ms) (DF)	τ (ms) (RTP)	Φ (%)
$NPhBF_2$-0.5% melt-cast sample	505(TTA) 585(RTP)	106(21.2%) 286(78.5%)	261	60.0
$N\alpha NBF_2$-0.5% melt-cast sample	510(TTA) 590(RTP)	181(21.8%) 352(68.2%)	275	42.2
$N\beta NBF_2$-0.5% melt-cast sample	515(TTA) 595(RTP)	166(31.8%) 327(68.2%)	250	40.1

The total emission of the samples, for example, the $N\beta NBF_2$–MeOBP-0.5% afterglow materials, consists of prompt fluorescence, delayed fluorescence and room-temperature phosphorescence. Although the fluorescence components are much larger than the phosphorescence components in the steady-state emission spectra such as the spectra of $N\beta NBF_2$–MeOBP afterglow materials as shown in Fig. 3C, the delayed fluorescence plus phosphorescence constitute a large percent of the total emission as estimated from the intensity integral of both fluorescence and phosphorescence decay (Fig. S20, ESI†). The emission decay profiles of $N\beta NBF_2$–MeOBP-0.5% afterglow materials monitored at 515 nm and 595 nm have been collected by TCSPC techniques (Fig. S20, ESI†). The emission decay of $N\beta NBF_2$–MeOBP-0.5% afterglow materials monitored at 515 nm can be fit into a triple-exponential decay with τ_1 of 30 ms (16.5%), τ_2 of 203 ms (52.5%) and τ_3 of 681 ms (31.0%) (Fig. S20, ESI†). Similar to the reported studies,[40,62] the prompt fluorescence lifetimes (the τ_1 part) measured using a microsecond flash lamp are in millisecond regimes. The accurate lifetimes of prompt fluorescence of $N\beta NBF_2$–MeOBP-0.5% afterglow materials have been measured using a picosecond pulsed diode laser to be τ_1 = 1.9 ns (29.5%) and τ_2 = 6.5 ns (70.5%) (Fig. S20, ESI†). The τ_2 and τ_3 parts can be assigned to delayed fluorescent components, which constitute 83.5% of the total fluorescence. The emission decay monitored at 595 nm can be fit into a triple-exponential decay with τ_1 of 3.7 ms (1.5%), τ_2 of 77.9 ms (22.3%) and τ_3 of 289 ms (76.2%) (Fig. S20, ESI†). The τ_2 and τ_3 parts contribute to afterglow behaviors, which constitute 98.5% of the total phosphorescence (Text S2, ESI†).

Other BF_2bdk–MeOBP materials have also been found to show long-lived emission characteristics when monitored at RTP and TTA regions (Fig. S21–S24, ESI†). The photoluminescence quantum yields (PLQYs) of BF_2bdk–MeOBP materials have been measured to be in the range of 40%–60% using a Hamamatsu absolute PLQY measurement system based on a standard protocol (Table 2). Fig. S1–S4 (ESI†) show that it is challenging to achieve highly efficient organic afterglow materials with long emission wavelengths. The PLQYs and afterglow lifetimes of the present long-emission-wavelength systems (Table 2) are among the highest values in the reported studies (Fig. S1–S4, ESI†). The TTA mechanism that can harvest triplet energies is of crucial importance to enhance organic afterglow efficiency.[7–15] The k_{TTA} values can be estimated from the delayed fluorescence lifetimes to be on the order of 10^0–10^1 s^{-1}, similar to the rate constants of phosphorescence decay. These moderate k_{TTA} values are necessary to improve afterglow efficiency and simultaneously maintain afterglow lifetimes.

Enhancing red organic afterglow efficiency *via* TADF

For the fabrication of red organic afterglow materials, molecular systems with low energy levels of excited states are required.

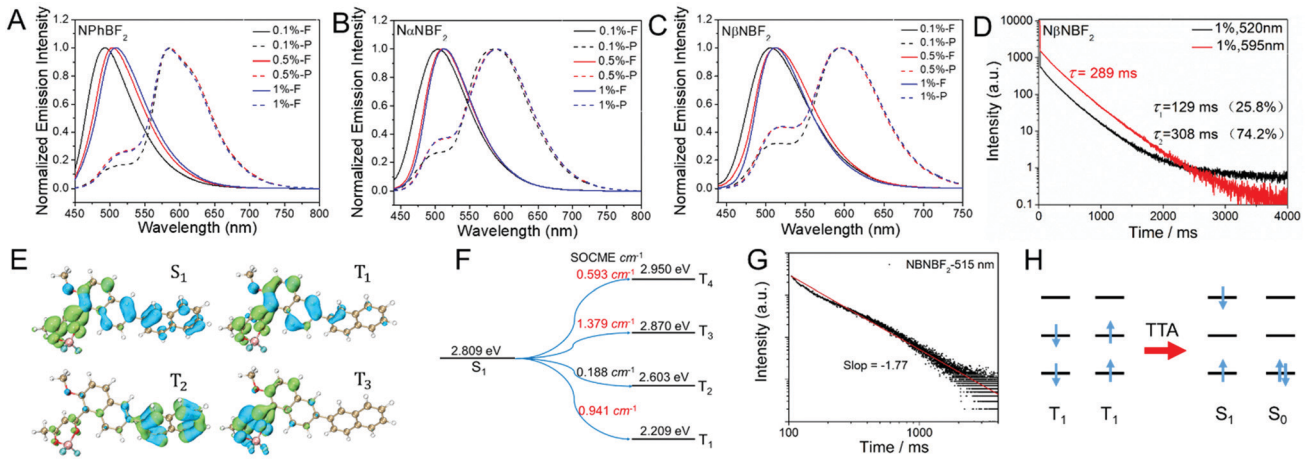

Fig. 3 (A–C) The room-temperature emission spectra collected in fluorescence mode and phosphorescence mode (1 ms delay) of (A) $NPhBF_2$–MeOBP, (B) $N\alpha NBF_2$–MeOBP and (C) $N\beta NBF_2$–MeOBP afterglow materials with weight ratios fixed at 0.1%, 0.5% and 1%, respectively. The spectra collected in fluorescence mode denote steady-state emission spectra. The spectra collected in phosphorescence mode represent delayed emission spectra that contain both phosphorescence and delayed fluoresence. (D) The room-temperature emission decay of $N\beta NBF_2$–MeOBP-1% afterglow materials monitored at 520 nm and 595 nm, respectively. (E) The isosurface maps of $N\beta NBF_2$ singlet and triplet excited states based on the TD-DFT calculated results. Blue and green isosurfaces correspond to hole and electron distributions, respectively. (F) TD-DFT calculated energy levels of $N\beta NBF_2$ singlet and triplet excited states and their spin–orbit coupling matrix elements (SOCME). (G) The double logarithmic plot of the room-temperature emission decay profile of $N\beta NBF_2$–MeOBP-0.5% afterglow materials monitored at 515 nm. (H) Schematic illustration of the TTA mechanism.

However, due to the energy gap law, all the related photophysical processes such as radiative decay and nonradiative decay would be increased in the systems with low energy levels of excited states.[69–71] As a result, the increased nonradiative decay would compete with radiative decay, and meanwhile the increase of radiative decay and nonradiative decay would shorten the emission lifetimes of the organic systems, both of which are detrimental to the fabrication of highly efficient red afterglow materials.

In the present study, it is found that $NPhRedBF_2$–MeOBP-0.01% materials exhibit orange red afterglow under ambient conditions upon ceasing the excitation source (Fig. S14, ESI†). The steady-state emission spectra of $NPhRedBF_2$–MeOBP materials display a fluorescence band in the range of 525 nm–725 nm with emission maxima at around 600 nm (Fig. 4A). Interestingly, the room-temperature phosphorescence spectra show nearly identical delayed fluorescence bands to those of the steady-state fluorescence spectra, which suggests a TADF mechanism in the dopant–matrix system. The emission decay profile as shown in Fig. 4B can be fit into τ_1 = 33 ms (69.3%), τ_2 = 117 ms (19.2%), and τ_3 = 313 ms (11.5%). Afterglow emission of $NPhRedBF_2$–MeOBP materials can be obtained by visible light excitation (Fig. S25, ESI†) and 530 nm laser excitation (Fig. S26, ESI†). This indicates that the contribution of energy transfer from MeOBP triplets to $NPhRedBF_2$ dopants is not necessary for the emergence of organic afterglow in the $NPhRedBF_2$–MeoBP system,[72,73] because MeOBP possesses insignificant absorption in the visible region (Fig. S27, ESI†). Besides, at such a low doping concentration, delayed fluorescence from TTA should not have such a large contribution to dominate the whole delayed fluorescence spectra. It is noted that boron difluoride curcuminoid and hemicurcuminoid

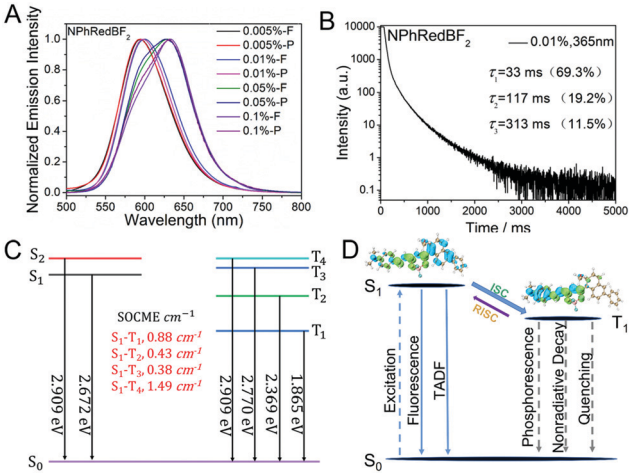

Fig. 4 (A) Room-temperature steady-state emission and delayed emission spectra of $NPhRedBF_2$–MeOBP afterglow materials at different doping concentrations. (B) Room-temperature emission decay of $NPhRedBF_2$–MeOBP-0.01% afterglow materials excited at 365 nm and monitored at 599 nm. (C) and (D) Schematic representations of (C) energy levels and spin orbital coupling matrix elements and (D) the proposed mechanism of organic afterglow in the $NPhRedBF_2$–MeOBP system.

compounds have been found to show TADF behaviours in several reported studies.[74–77] In addition, due to the presence of two or multiple electron-donating functional groups, the types of ICT excited states of $NPhRedBF_2$ can be enriched. The nature of some triplet states may be different from that of the S_1 state, so ISC and RISC can be accelerated to some extent according to the El-Sayed rule. Moreover, TD-DFT calculations, where multiple ISC channels show relatively larger SOCME

values and some of these channels possess relatively small ΔE_{ST} values, support that the organic systems possess a moderate tendency of RISC (Fig. 4C, Fig. S28, ESI†). It has been found that the afterglow colour of NPhRedBF$_2$–MeOBP-0.01% materials at 77 K (red afterglow from phosphorescence decay of triplet states, Fig. S16D, ESI†) shows red-shifted behaviours when compared to that at room temperature (orange red, Fig. S14, ESI†), which suggests that the TADF mechanism is frozen at 77 K. Similar to the NPhRedBF$_2$–MeOBP materials, NPhRedBF$_2$–benzophenone materials also exhibit TADF-type organic afterglow properties under ambient conditions (Fig. S29, ESI†). The MeOBP matrices showed strong phosphorescence from 77 K to 240 K and thus largely interfered with the temperature-dependent phosphorescence measurements as reported in our recent study;[78] so benzophenone (BP) matrices were used in the place of MeOBP. At 77 K, the phosphorescence spectra of NPhRedBF$_2$–benzophenone materials have been found to exhibit a structured emission band ranging from 630 nm to 850 nm with emission maxima at 658 nm (Fig. 5). This 630–850 nm emission band can be attributed to phosphorescence decay of NPhRedBF$_2$ triplets within the benzophenone matrices. Upon increasing the temperature, the delayed fluorescence bands at approximately 580 nm gradually increase and dominate the whole delayed emission spectra at 300 K (Fig. 5). These studies further support the TADF mechanism of NPhRedBF$_2$–matrix afterglow materials, since the RISC process that is the rate-determining step for TADF is frozen at 77 K and can be activated at room temperature. All the above observations and analysis support our proposed TADF mechanism in the dopant–matrix systems. The triplet excited states can undergo reverse intersystem crossing to reach singlet excited states and subsequently emit delayed fluorescence, which can significantly enhance the organic afterglow efficiency of the red afterglow systems (Fig. 4D). The k_{TADF} values can be estimated from the delayed fluorescence lifetimes to be on the order of 10^0–10^2 s^{-1}. When compared to the TADF emitters with large k_{TADF} values of 10^3–10^6 s^{-1},[16–23,59,60] the moderate k_{TADF} values are a distinct feature of the present study different from those of the TADF emitters for efficient OLEDs. Organic afterglow systems with moderate k_{TADF} values can simultaneously harvest triplet energies by the TADF mechanism and maintain afterglow lifetimes. The PLQYs of NPhRedBF$_2$–MeOBP materials at 0.005%, 0.05% and 0.5% doping concentrations have been determined to be 56.3%, 18.6% and 6.5%, respectively; the decrease of PLQY upon increasing the doping concentration can be caused by aggregation of NPhRedBF$_2$ molecules in MeOBP matrices. NPhRedBF$_2$–MeOBP-0.005% afterglow materials with such high PLQYs have been rarely achieved in the reported studies (Fig. S1–S4, ESI†).

By increasing the doping concentration, the fluorescence spectra of the NPhRedBF$_2$–MeOBP materials show the emergence of an even lower-energy emission signal at 631 nm (Fig. 4A and 6), which can be attributed to molecular aggregation in the dopant–matrix systems; most BF$_2$bdk systems show red-shifted emission upon molecular aggregation.[61–64] In the delayed fluorescence spectra, the lower-energy emission bands at 631 nm persist (Fig. 4A and 5), indicating that the delayed fluorescence bands can be readily adjusted by increasing the doping concentration to red regions.

The role of organic matrices in dopant–matrix afterglow systems

The role of organic matrices for the emergence of organic afterglow under ambient conditions is an open question in the research fields of room-temperature phosphorescence and organic afterglow systems. It has been reported that triplet-to-triplet excited state energy transfers from organic matrices to luminescent dopants can give rise to organic afterglow.[72,73] In the present study, the BF$_2$bdk–MeOBP materials can be excited by 420 nm visible light to exhibit organic afterglow (Fig. 3A–C). In particular, in the case of the NPhRedBF$_2$–MeOBP system, afterglow can be observed by 530 nm excitation (Fig. S26, ESI†). Since MeOBP possesses insignificant absorption in the visible region (Fig. S27, ESI†), we argue that triplet-to-triplet excited state energy transfer is not necessary for the formation of dopant–matrix afterglow materials in the present systems.

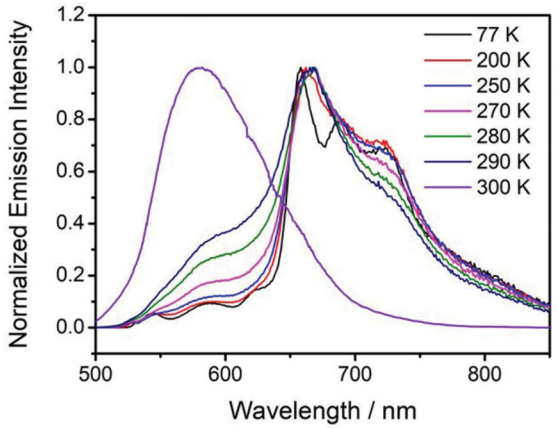

Fig. 5 Temperature-dependent delayed emission spectra of NPhRedBF$_2$–benzophenone samples.

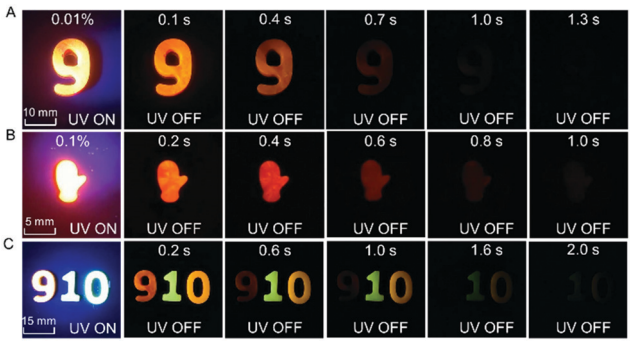

Fig. 6 Photographs of afterglow objects with desired shapes prepared by the melt casting technique of (A) NPhRedBF$_2$–MeOBP-0.01%, (B) NPhRedBF$_2$–MeOBP-0.1% and (C) (left–right) NPhRedBF$_2$–MeOBP-0.01%, NαN–MeOBP-0.5% and NβNBF$_2$–MeOBP-0.5% under 365 nm UV light and after removal of the UV light.

Several recently reported studies proposed that organic matrices with T_1 levels sandwiched between S_1 and T_1 levels of luminescent dopants can serve as bridges for the singlet-to-triplet intersystem crossing of the luminescent dopants, giving rise to room-temperature organic afterglow.[38,51] This is not the case in the present study, because the naphthalene-containing BF_2bdk luminescent dopants, especially in the NPhRedBF_2 system, possess lower S_1 and T_1 levels than the T_1 level of MeOBP matrices. With reference to the studies of Adachi's group and our research group, a high T_1 level of organic matrices is necessary to avoid afterglow quenching caused by triplet-to-triplet energy transfer from luminescent dopants to organic matrices.[62,79]

On the basis of our previous study[52,61,62] and the current findings, we propose that the MeOBP matrices with large dipole moments can interact with and perturb the excited states of naphthalene-containing BF_2bdk luminescent dopants *via* dipole–dipole interactions. These interactions can stabilize the singlet excited states of the luminescent dopants and consequently reduce ΔE_{ST} given that the energy level of BF_2bdk triplets is less affected by organic matrices, leading to the enhancement of intersystem crossing of BF_2bdk excited states; in the case of NPhRedBF_2, reverse intersystem crossing can also be enhanced. Meanwhile, the MeOBP matrices can inhibit nonradiative decay of BF_2bdk triplets by their rigid microenvironments and protect BF_2bdk triplets from oxygen quenching by encapsulation. This is our understanding on the role of organic matrices for the fabrication of dopant–matrix afterglow materials. In control experiments without the presence of MeOBP matrices, the TADF property of NPhRedBF_2 has not been observed in the solution state (Fig. S30, ESI†).

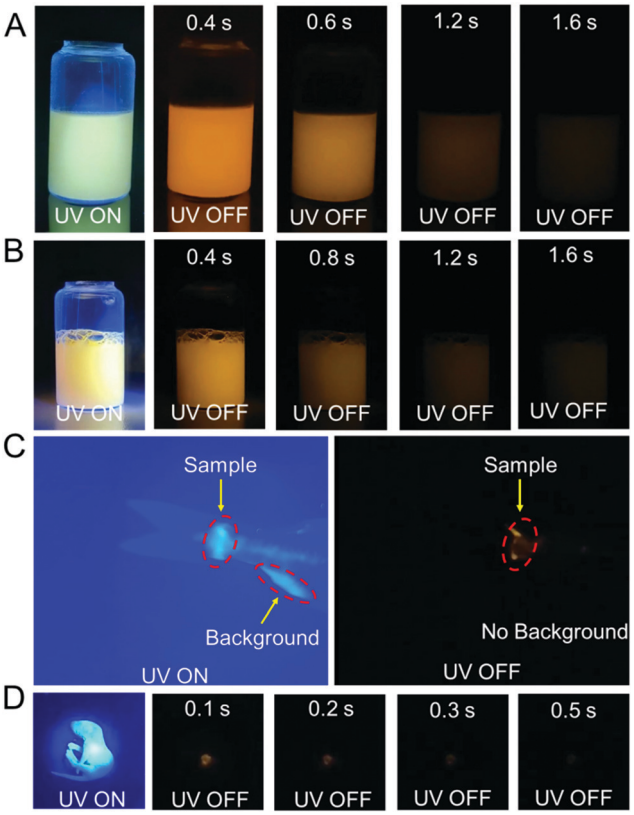

Fig. 7 (A) and (B) Photographs of (A) NβNBF_2–MeOBP-0.5% and (B) NβNBF_2–MeOBP-0.5% + R6G afterglow dispersion under 365 nm UV light and after removal of the UV light. (C) and (D) Preliminary bioimaging studies of the NβNBF_2–MeOBP-0.5% afterglow dispersion in living (C) fish and (D) mice.

Functionalities of the dopant–matrix afterglow materials

Because of the relatively low melting points of MeOBP matrices, the afterglow materials can be processed into objects with desired shapes by the melt casting technique with the aid of silicone moulds (Fig. 2, 6 and Fig. S31, ESI†). Fig. 6C shows the combination of afterglow numbers with different emission colours prepared from NPhRedBF_2–MeOBP-0.01%, NαN–MeOBP-0.5% and NβNBF_2–MeOBP-0.5% materials, where NαN represents 6-methoxy-1,2′-binaphthalene. By taking advantage of the different shapes, different afterglow colours and different afterglow duration times, the combination of these materials shows the potential for the fabrication of multicolour-encoded anti-counterfeiting labels or devices.[24–38]

For most biomedical applications, the afterglow materials should be processed into aqueous dispersions. However, it is found that, in many reported studies, these processing procedures can lead to a significant decrease or complete loss of the afterglow properties in the material systems. In the present study, we were inspired by the widely used technique for the preparation of emulsions and suspensions. Pluronic F-127 surfactants have been used to disperse hydrophobic NβNBF_2–MeOBP materials. Since the NβNBF_2–MeOBP materials are in solid states at room temperature, we first melt the materials by heating to 65 °C and then inject the molten samples into a hot aqueous solution (80 °C) of Pluronic F-127 surfactants under sonication. It is found that the sonication can efficiently disperse the molten samples into very small droplets that can be stabilized by Pluronic F-127 surfactants to form a milky dispersion. The hot milky dipsersion exhibits fluorescence properties under 365 nm UV light but shows no afterglow upon swithching off the UV light; in the molten state, the molecular motion of NβNBF_2 should be very active, so nonradiative decay can quench the triplet states of NβNBF_2 molecules. After rapid cooling, the aqueous dispersion displays orange afterglow with a duration of 1.6 s as observed by human eyes in a dark room (Fig. 7A). These observations indicate that, by the processing methods in the present study, an aqueous disperison of room-temperature organic afterglow materials can be readily obtained without the use of organic solvents or expensive equipment.

Due to their long-lived emission characteristics, the capability of NβNBF_2–MeOBP afterglow dispersions in avoiding the interference of background fluorescence has been tested. Rhodamine 6G has been added to the afterglow dispersions of NβNBF_2–MeOBP materials. In the UV-on state, only yellow fluorescence from rhodamine 6G has been observed. In the UV-off state, the yellow fluorescence disappears immediately, whereas the aqueous dispersion exhibits orange afterglow that

is originated from NβNBF$_2$–MeOBP materials (Fig. 7B). These observations indicate that the aqueous afterglow materials possess intriguing properties to eliminate background interference *via* a time-gated imaging mode. Furthermore, preliminary *in vivo* bioimaging studies have been performed. The aqueous afterglow dispersion can be readily drawn by syringes and injected into animal tissues. After injecting into fish tails, the bioimaging is found to be interfered with by the fluorescence from the anal fin in the UV-on mode, while this interference can be completely removed in the UV-off mode where only NβNBF$_2$–MeOBP materials show afterglow emission (Fig. 7C). The preliminary bioimaging studies on mice also show very clean background in the UV-off state (Fig. 7D). These studies suggest that, because of their long-lived excited state nature, the aqueous afterglow materials show promising applications in biomedical fields.

Conclusions

In conclusion, the present study demonstrates that triplet–triplet annihilation and thermally-activated delayed fluorescence mechanisms can be incorporated into organic room-temperature phosphorescence systems to remarkably enhance the afterglow quantum efficiency of the material systems under ambient conditions. A distinct feature of the present study is the moderate or modest rate constants of triplet–triplet annihilation and thermally-activated delayed fluorescence, which can significantly improve the afterglow efficiency and simultaneously maintain long afterglow lifetimes.

The molecular design of luminescent dopants is very simple; naphthalene-containing BF$_2$bdk compounds are selected to increase the quantum yields of intersystem crossing and molar absorption coefficients for the significant population of triplet excited states. The organic matrices with large molecular dipole moments are also readily available and very cheap. The organic matrices not only suppress nonradiative decay and quenching but also facilitate forward and reverse intersystem crossing *via* dipole–dipole interactions. These endow great opportunities to the dopant–matrix design strategy for the fabrication of high-performance organic afterglow materials.

Because of the flexibility of component selection of the dopant–matrix design strategy, it is anticipated that diverse organic afterglow materials with intriguing photophysical properties can be obtained. We also envisage that these afterglow materials can be widely used in fields such as data storage and encryption, as well as high-contrast bioimaging and highly sensitive optical analyses.

Experimental

Preparation of organic afterglow materials

For the preparation of the BF$_2$bdk–MeOBP materials, naphthalene-containing BF$_2$bdk in dichloromethane solution and MeOBP in dichloromethane solution were first added into an agate mortar. After grinding and solvent evaporation, BF$_2$bdk–MeOBP afterglow powders were obtained. Other afterglow materials with different doping concentrations, different BF$_2$bdk dopants and different organic matrices were prepared through similar processes. For the preparation of melt-cast afterglow objects with desired shapes, the BF$_2$bdk–MeOBP powders were first heated to form molten mixtures, and then poured into silicone moulds with desired shapes. After cooling to room temperature, afterglow objects with various shapes were obtained.

Conflicts of interest

There are no conflicts to declare.

Acknowledgements

We acknowledge the financial support from the National Natural Science Foundation of China (22175194), Shanghai Scientific and Technological Innovation Project (20QA1411600, 20ZR1469200), and Hundred Talents Program from Shanghai Institute of Organic Chemistry (Y121078).

Notes and references

1 V. W.-W. Yam, V. K.-M. Au and S. Y.-L. Leung, *Chem. Rev.*, 2015, **115**, 7589–7728.
2 O. Bolton, K. Lee, H.-J. Kim, K. Y. Lin and J. Kim, *Nat. Chem.*, 2011, **3**, 205–210.
3 G. Zhang, G. M. Palmer, M. W. Dewhirst and C. L. Fraser, *Nat. Mater.*, 2009, **8**, 747–751.
4 W. Z. Yuan, X. Y. Shen, H. Zhao, J. W. Lam, L. Tang, P. Lu, C. Wang, Y. Liu, Z. Wang and Q. Zheng, *J. Phys. Chem. C*, 2010, **114**, 6090–6099.
5 T. Zou, C. T. Lum, C.-N. Lok, J.-J. Zhang and C.-M. Che, *Chem. Soc. Rev.*, 2015, **44**, 8786–8801.
6 J. Mei, N. L. Leung, R. T. Kwok, J. W. Lam and B. Z. Tang, *Chem. Rev.*, 2015, **115**, 11718–11940.
7 X. Qiao and D. Ma, *Mater. Sci. Eng., R*, 2020, **139**, 100519.
8 F. B. Dias, K. N. Bourdakos, V. Jankus, K. C. Moss, K. T. Kamtekar, V. Bhalla, J. Santos, M. R. Bryce and A. P. Monkman, *Adv. Mater.*, 2013, **25**, 3707–3714.
9 R. Ieuji, K. Goushi and C. Adachi, *Nat. Commun.*, 2019, **10**, 5283.
10 T.-A. Lin, C. F. Perkinson and M. A. Baldo, *Adv. Mater.*, 2020, **32**, 1908175.
11 B. Joarder, N. Yanai and N. Kimizuka, *J. Phys. Chem. Lett.*, 2018, **9**, 4613–4624.
12 S. M. Suresh, E. Duda, D. Hall, Z. Yao, S. Bagnich, A. M. Z. Slawin, H. Bässler, D. Beljonne, M. Buck, Y. Olivier, A. Köhler and E. Zysman-Colman, *J. Am. Chem. Soc.*, 2020, **142**, 6588–6599.
13 K. J. Fallon, E. M. Churchill, S. N. Sanders, J. Shee, J. L. Weber, R. Meir, S. Jockusch, D. R. Reichman,

M. Y. Sfeir, D. N. Congreve and L. M. Campos, *J. Am. Chem. Soc.*, 2020, **142**, 19917–19925.
14 Y. C. Simon and C. Weder, *J. Mater. Chem.*, 2012, **22**, 20817–20830.
15 D. Yang, J. Han, M. Liu and P. Duan, *Adv. Mater.*, 2019, **31**, 1805683.
16 H. Uoyama, K. Goushi, K. Shizu, H. Nomura and C. Adachi, *Nature*, 2012, **492**, 234–238.
17 Q. Zhang, B. Li, S. Huang, H. Nomura, H. Tanaka and C. Adachi, *Nat. Photonics*, 2014, **8**, 326–332.
18 Y. Tao, K. Yuan, T. Chen, P. Xu, H. Li, R. Chen, C. Zheng, L. Zhang and W. Huang, *Adv. Mater.*, 2014, **26**, 7931–7958.
19 M. Y. Wong and E. Zysman-Colman, *Adv. Mater.*, 2017, **29**, 1605444.
20 Y. Liu, C. Li, Z. Ren, S. Yan and M. R. Bryce, *Nat. Rev. Mater.*, 2018, **3**, 18020.
21 Y. Im, M. Kim, Y. J. Cho, J.-A. Seo, K. S. Yook and J. Y. Lee, *Chem. Mater.*, 2017, **29**, 1946–1963.
22 Z. Yang, Z. Mao, Z. Xie, Y. Zhang, S. Liu, J. Zhao, J. Xu, Z. Chi and M. P. Aldred, *Chem. Soc. Rev.*, 2017, **46**, 915–1016.
23 W. Li, Z. Li, C. Si, M. Y. Wong, K. Jinnai, A. K. Gupta, R. Kabe, C. Adachi, W. Huang, E. Zysman-Colman and I. D. W. Samuel, *Adv. Mater.*, 2020, **32**, 2003911.
24 W. Zhao, Z. He and B. Z. Tang, *Nat. Rev. Mater.*, 2020, **5**, 869–885.
25 N. Gan, H. Shi, Z. An and W. Huang, *Adv. Funct. Mater.*, 2018, **28**, 1802657.
26 X. Ma, J. Wang and H. Tian, *Acc. Chem. Res.*, 2019, **52**, 738–748.
27 S. Hirata, *Adv. Opt. Mater.*, 2017, **5**, 1700116.
28 A. Forni, E. Lucenti, C. Botta and E. Cariati, *J. Mater. Chem. C*, 2018, **6**, 4603–4626.
29 Kenry, C. Chen and B. Liu, *Nat. Commun.*, 2019, **10**, 2111.
30 Z. An, C. Zheng, Y. Tao, R. Chen, H. Shi, T. Chen, Z. Wang, H. Li, R. Deng, X. Liu and W. Huang, *Nat. Mater.*, 2015, **14**, 685–690.
31 C. Chen, Z. Chi, K. C. Chong, A. S. Batsanov, Z. Yang, Z. Mao, Z. Yang and B. Liu, *Nat. Mater.*, 2021, **20**, 175–180.
32 X.-F. Wang, H. Xiao, P.-Z. Chen, Q.-Z. Yang, B. Chen, C.-H. Tung, Y.-Z. Chen and L.-Z. Wu, *J. Am. Chem. Soc.*, 2019, **141**, 5045–5050.
33 Y. Wang, J. Yang, M. Fang, Y. Yu, B. Zou, L. Wang, Y. Tian, J. Cheng, B. Z. Tang and Z. Li, *Matter*, 2020, **3**, 449–463.
34 Z. Mao, Z. Yang, Y. Mu, Y. Zhang, Y.-F. Wang, Z. Chi, C.-C. Lo, S. Liu, A. Lien and J. Xu, *Angew. Chem., Int. Ed.*, 2015, **54**, 6270–6273.
35 X. Zhen, Y. Tao, Z. An, P. Chen, C. Xu, R. Chen, W. Huang and K. Pu, *Adv. Mater.*, 2017, **29**, 1606665.
36 Y. Yu, M. S. Kwon, J. Jung, Y. Zeng, M. Kim, K. Chung, J. Gierschner, J. H. Youk, S. M. Borisov and J. Kim, *Angew. Chem., Int. Ed.*, 2017, **56**, 16207–16211.
37 Y. Lei, W. Dai, J. Guan, S. Guo, F. Ren, Y. Zhou, J. Shi, B. Tong, Z. Cai, J. Zheng and Y. Dong, *Angew. Chem., Int. Ed.*, 2020, **59**, 16054–16060.
38 Z. Xie, X. Zhang, H. Wang, C. Huang, H. Sun, M. Dong, L. Ji, Z. An, T. Yu and W. Huang, *Nat. Commun.*, 2021, **12**, 3522.
39 W. Zhao, Z. He, J. W. Y. Lam, Q. Peng, H. Ma, Z. Shuai, G. Bai, J. Hao and B. Z. Tang, *Chem*, 2016, **1**, 592–602.
40 J. Jin, H. Jiang, Q. Yang, L. Tang, Y. Tao, Y. Li, R. Chen, C. Zheng, Q. Fan, K. Y. Zhang, Q. Zhao and W. Huang, *Nat. Commun.*, 2020, **11**, 842.
41 Z. Yang, C. Xu, W. Li, Z. Mao, X. Ge, Q. Huang, H. Deng, J. Zhao, F. L. Gu, Y. Zhang and Z. Chi, *Angew. Chem., Int. Ed.*, 2020, **59**, 17451–17455.
42 J. Wang, X. Gu, H. Ma, Q. Peng, X. Huang, X. Zheng, S. H. P. Sung, G. Shan, J. W. Y. Lam, Z. Shuai and B. Z. Tang, *Nat. Commun.*, 2018, **9**, 2963.
43 H. Ma, Q. Peng, Z. An, W. Huang and Z. Shuai, *J. Am. Chem. Soc.*, 2019, **141**, 1010–1015.
44 Z.-Y. Zhang, Y. Chen and Y. Liu, *Angew. Chem., Int. Ed.*, 2019, **58**, 6028–6032.
45 L. Bian, H. Shi, X. Wang, K. Ling, H. Ma, M. Li, Z. Cheng, C. Ma, S. Cai, Q. Wu, N. Gan, X. Xu, Z. An and W. Huang, *J. Am. Chem. Soc.*, 2018, **140**, 10734–10739.
46 J. Wang, Z. Huang, X. Ma and H. Tian, *Angew. Chem., Int. Ed.*, 2020, **59**, 9928–9933.
47 P. Wei, X. Zhang, J. Liu, G.-G. Shan, H. Zhang, J. Qi, W. Zhao, H. H.-Y. Sung, I. D. Williams, J. W. Y. Lam and B. Z. Tang, *Angew. Chem., Int. Ed.*, 2020, **59**, 9293–9298.
48 S. Hirata, K. Totani, J. Zhang, T. Yamashita, H. Kaji, S. R. Marder, T. Watanabe and C. Adachi, *Adv. Funct. Mater.*, 2013, **23**, 3386–3397.
49 I. Bhattacharjee and S. Hirata, *Adv. Mater.*, 2020, **32**, 2001348.
50 H. Wu, W. Chi, Z. Chen, G. Liu, L. Gu, A. K. Bindra, G. Yang, X. Liu and Y. Zhao, *Adv. Funct. Mater.*, 2019, **29**, 1807243.
51 S. Guo, W. Dai, X. Chen, Y. Lei, J. Shi, B. Tong, Z. Cai and Y. Dong, *ACS Mater. Lett.*, 2021, **3**, 379–397.
52 Y. Sun, G. Wang, X. Li, B. Zhou and K. Zhang, *Adv. Opt. Mater.*, 2021, **9**, 2100353.
53 R. Kabe and C. Adachi, *Nature*, 2017, **550**, 384–387.
54 P. Alam, N. L. C. Leung, J. Liu, T. S. Cheung, X. Zhang, Z. He, R. T. K. Kwok, J. W. Y. Lam, H. H. Y. Sung, I. D. Williams, C. C. S. Chan, K. S. Wong, Q. Peng and B. Z. Tang, *Adv. Mater.*, 2020, **32**, 2001026.
55 Y. Wang, H. Gao, J. Yang, M. Fang, D. Ding, B. Z. Tang and Z. Li, *Adv. Mater.*, 2021, **33**, 2007811.
56 Y. Lei, W. Dai, Y. Tian, J. Yang, P. Li, J. Shi, B. Tong, Z. Cai and Y. Dong, *J. Phys. Chem. Lett.*, 2019, **10**, 6019–6025.
57 Y. Wang, H. Gao, J. Yang, M. Fang, D. Ding, B. Z. Tang and Z. Li, *Adv. Mater.*, 2021, **33**, 2007811.
58 B. Chen, W. Huang, X. Nie, F. Liao, H. Miao, X. Zhang and G. Zhang, *Angew. Chem., Int. Ed.*, 2021, **60**, 16970–16973.
59 P. K. Samanta, D. Kim, V. Coropceanu and J.-L. Brédas, *J. Am. Chem. Soc.*, 2017, **139**, 4042–4051.
60 H. Noda, X.-K. Chen, H. Nakanotani, T. Hosokai, M. Miyajima, N. Notsuka, Y. Kashima, J.-L. Brédas and C. Adachi, *Nat. Mater.*, 2019, **18**, 1084–1090.
61 B. Zhou, G. Wang, X. Wang, W. Guo, J. Li and K. Zhang, *J. Mater. Chem. C*, 2021, **9**, 3939–3947.
62 X. Wang, Y. Sun, G. Wang, J. Li, X. Li and K. Zhang, *Angew. Chem., Int. Ed.*, 2021, **60**, 17138–17147.

63 P.-Z. Chen, L.-Y. Niu, Y.-Z. Chen and Q.-Z. Yang, *Coord. Chem. Rev.*, 2017, **350**, 196–216.
64 C.-T. Poon, W. H. Lam, H.-L. Wong and V. W.-W. Yam, *J. Am. Chem. Soc.*, 2010, **132**, 13992–13993.
65 S. K. Behera, S. Y. Park and J. Gierschner, *Angew. Chem., Int. Ed.*, 2020, **60**, 22624–22638.
66 N. A. Kukhta and M. R. Bryce, *Mater. Horiz.*, 2021, **8**, 33–55.
67 J. Chen, X. Chen, Y. Liu, J. Zhao, Z. Yang, Y. Zhang and Z. Chi, *Chem. Sci.*, 2021, **12**, 9201–9206.
68 G. N. Lewis and M. Kasha, *J. Am. Chem. Soc.*, 1944, **66**, 2100–2116.
69 J. V. Caspar and T. J. Meyer, *J. Phys. Chem.*, 1983, **87**, 952–957.
70 R. Englman and J. Jortner, *J. Lumin.*, 1970, **1**, 134–142.
71 J. V. Caspar, E. M. Kober, B. P. Sullivan and T. J. Meyer, *J. Am. Chem. Soc.*, 1982, **104**, 630–632.
72 J. Wang, H. Zhang, L.-Y. Niu, X. Zhu, Y.-F. Kang, R. Boulatov and Q.-Z. Yang, *CCS Chem.*, 2020, **2**, 1391.
73 K. Jinnai, R. Kabe and C. Adachi, *Adv. Mater.*, 2018, **30**, 1800365.
74 D.-H. Kim, A. D'Aléo, X.-K. Chen, A. D. S. Sandanayaka, D. Yao, L. Zhao, T. Komino, E. Zaborova, G. Canard, Y. Tsuchiya, E. Choi, J. W. Wu, F. Fages, J.-L. Brédas, J.-C. Ribierre and C. Adachi, *Nat. Photonics*, 2018, **12**, 98–104.
75 N. R. Paisley, S. V. Halldorson, M. V. Tran, R. Gupta, S. Kamal, W. R. Algar and Z. M. Hudson, *Angew. Chem., Int. Ed.*, 2021, **60**, 18630–18638.
76 A. Shahalizad, A. Malinge, L. Hu, G. Laflamme, L. Haeberlé, D. M. Myers, J. Mao, W. G. Skene and S. Kéna-Cohen, *Adv. Funct. Mater.*, 2020, **31**, 2007119.
77 A. D'Aléo, M. H. Sazzad, D. H. Kim, E. Y. Choi, J. W. Wu, G. Canard, F. Fages, J.-C. Ribierre and C. Adachi, *Chem. Commun.*, 2017, **53**, 7003–7006.
78 Y. Sun, J. Liu, J. Li, X. Li, X. Wang, G. Wang and K. Zhang, *Adv. Opt. Mater.*, 2021, 2101909.
79 N. Notsuka, R. Kabe, K. Goushi and C. Adachi, *Adv. Funct. Mater.*, 2017, **27**, 1703902.

